Russian Journal of Earth Sciences

Variation of Total Electron Content Over Nepal During Geomagnetic Storms: GPS Observations

A. Silwal[*,1], S. P. Gautam[1], P. Poudel[2], M. Karki[1], N. P. Chapagain[3], and B. Adhikari[4]

[1]Department of Space Science, University of Alabama in Huntsville, Huntsville, AL, USA
[2]Patan Multiple Campus, Tribhuvan University, Lalitpur, Nepal
[3]Amrit Campus, Tribhuvan University, Kathmandu, Nepal
[4]Department of Physics, St. Xavier College, Maitighar, Kathmandu, Nepal
* **Correspondence to:** Ashok Silwal, ashoksilwal0@gmail.com

Abstract: Geomagnetic storms have very profound effects on the Total Electron Content (TEC) of the ionosphere. In order to investigate the equatorial and low-latitude ionospheric response to the geomagnetic storms of varying intensities, a detailed study of vertical TEC (VTEC) variations resulting from Global Positioning System (GPS) data acquired at four GPS stations in Nepal along 80°–90 °E longitude and 26°–30 °N latitude sector has been carried out in the present work. The results were analyzed with other favorable inducing factors (solar wind parameters and geomagnetic indices) affecting TEC to constrain the causative factor. We observed a positive enhancement during all three events studied. During the severe geomagnetic storm event, the deviation was ~18 TECU, while it was recorded ~12 TECU and ~8 TECU during moderate and minor geomagnetic activity, respectively. The Detrended Cross-Correlation Analysis (DXA) illustrates that the hourly averaged VTEC of the BESI station was found to have a strong positive correlation with other stations in three storm events, indicating a similar response of all stations towards the geomagnetic storm. In addition, the correlation of VTEC with solar wind parameters and geomagnetic indices illustrated that the VTEC shows a good positive association with solar wind velocity (V_{sw}) in all three geomagnetic events. In contrast, the correlation of plasma density (N_{sw}), interplanetary magnetic field (IMF B_z), the symmetric horizontal component of geomagnetic field (*SYM-H*), and Geomagnetic Auroral Electrojet (*AE*) index with VTEC vary with the intensity of the storm. Overall results of the study have revealed the characteristic features of TEC variation over Nepal regions during magnetic storms, which validates earlier research on ionospheric responses to geomagnetic storms and theoretical assumptions.

Keywords: Total Electron Content (TEC), GPS, Geomagnetic storm, solar wind parameters, Cross-correlation

Citation: Silwal, A., S. P. Gautam, P. Poudel, M. Karki, N. P. Chapagain, and B. Adhikari (2023), Variation of Total Electron Content Over Nepal During Geomagnetic Storms: GPS Observations, *Russ. J. Earth. Sci.*, 23, ES3012, https://doi.org/10.2205/2023es000833

Research Article

Received: 16 January 2022
Accepted: 31 January 2023
Published: 17 September 2023

1. Introduction

The ionosphere is a dynamic layer of the Earth's upper atmosphere that consists of a high concentration of electrons and ions and generally changes according to the Sun's radiation [*Krypiak-Gregorczyk*, 2018]. It is an important part of near-Earth space that plays a crucial role in radio communication, global navigation satellite system (GNSS), radar detection, forecasting of space weather, and other systems using ionospheric electromagnetic wave signals [*Schrijver et al.*, 2015]. In the Earth's ionosphere, complex electrodynamic processes emerge as a result of spontaneous interactions between the neutral atmosphere and the ionospheric plasma [*de Abreu et al.*, 2017], which have a variety of consequences. In this case, it is controlled by the neutral winds of the upper atmosphere, which interact with the conductive and magnetic regions of the ionosphere and result in the generation of

electric fields in the ionospheric E and F regions due to the dynamo effect [*Abdu*, 2005; *Abdu et al.*, 2003]. The horizontal pressure gradient present in the atmosphere led to the development of dynamo electric fields in the E region as a result of variation in solar radiation absorption along geomagnetic field lines at high altitudes in the F region [*Panda et al.*, 2015]. During the daytime, the dynamo electric field E pointing eastward and the geomagnetic field **B** pointing northward at the dip equator gets mapped onto the F region through the $\mathbf{E} \times \mathbf{B}$ drift, bringing the plasma to higher altitudes in the equatorial region [*Abdu et al.*, 2003; *de Abreu et al.*, 2017; *Panda et al.*, 2015]. The plasma then diffuses down along the geomagnetic field lines into both hemispheres, generating two crests of plasma on either side of the geomagnetic equator, known as equatorial ionization anomaly (EIA) or Appleton anomaly [*Abdu*, 2005]. The overall process is known as the equatorial "fountain effect" [*Kelly et al.*, 2004]. The study of ionospheric behavior provides valuable insight into ionospheric temporal and spatial variations [*Zhang et al.*, 2018] and forecasting space weather.

When a strong southward interplanetary magnetic field (IMF) of the solar wind interacts with the northward geomagnetic field, the magnetospheric convection is enhanced through the magnetic merging process at the dayside magnetopause [*Adhikari et al.*, 2018; *Mendes et al.*, 2005]. Based on the enhanced magnetospheric convection, normally existing magnetospheric and ionospheric quiet currents are expanded and intensified due to an increased level of solar wind-magnetosphere coupling [*de Gonzalez et al.*, 2004; *Gonzalez et al.*, 1994; *Jankovičová et al.*, 2002]. At mid and low latitudes, the ring current dominates, whereas at higher latitudes, a system of ionospheric electrojet currents running horizontally in the auroral oval predominate and causes a geomagnetic storm or geomagnetic substorm, which is characterized by a significant depression of the H component of the geomagnetic field [*Kamide et al.*, 1998; *Shinbori et al.*, 2020; *Silwal et al.*, 2021a].

During a geomagnetic disturbance, noticeable changes in ionospheric characteristics such as composition, temperature, and circulation can be observed as a result of variations in solar wind velocity, temperature, and density, accompanied by significant changes in the north-south component of interplanetary magnetic field (IMF B_z) [*Shinbori et al.*, 2020]. During quiet periods, however, ground measurements do not reveal considerable disturbances [*Bhattarai et al.*, 2016; *Sharma et al.*, 2011]. During geomagnetic storms, the ionospheric electron density also fluctuates as a result of the magnetic field disturbances. Since the TEC is a measure of integrated electron density, significant changes in electron density are likely to be reflected in the TEC [*Davies*, 1990]. The positive storm effect or negative storm effect refers to the increase or decrease in electron density compared to quiet conditions [*Danilov*, 2001; *Fuller-Rowell et al.*, 1994]. Small-scale variations in plasma density create large fluctuations in the amplitude and phase of ionosphere radio signals, which is known as scintillation [*Chapagain*, 2016]. Large-scale oscillations and their related TEC variations can complicate phase ambiguity resolution, increase the probability of uncorrected cycle slips, and cause a failure in GNSS signal lock [*Mansilla*, 2019].

The ionospheric TEC is one of the important parameters to understand the phenomenon of space weather. TEC modeling is widely used in the fields of geodesy, communication, and positioning errors associated with GPS [*Hofmann-Wellenhof et al.*, 2012]. The ionospheric delay is proportional to TEC [*Hu et al.*, 2021; *Yao et al.*, 2021] and changes continually with space, time, solar, and geomagnetic activity. That is the primary reason why we can calculate the TEC from GPS data and use it to investigate various types of ionospheric phenomena [*Rastogi and Klobuchar*, 1990].

Four numerical simulations using the coupled thermosphere-ionosphere model were introduced by *Fuller-Rowell et al.* [1994], illustrating the ionospheric response to the geomagnetic storm. *Adhikari et al.* [2019] studied the solar superstorm of 18–22 November 2003. From their result, changes in TEC and *SYM-H* during the event provided an indication for the possible changes in the space weather caused by the solar superstorm. *Mansilla* [2019] observed both positive and negative TEC variations during some intense geomagnetic storms that occurred between 2012 and 2016. In addition, positive variations

were found to be significantly more prominent in the winter, and negative disturbances were discovered to be particularly long-lasting. *Ikubanni et al.* [2018] observed the increment of TEC by ~25% in African equatorial regions during St. Patrick's Day storms. In a recent study, *Shinbori et al.* [2020] investigated the temporal and spatial variations of TEC enhancements during the geomagnetic storms of September 27 and 28, 2017, and observed a clear increase in the ratio of the TEC difference from noon to afternoon at high latitudes within 1 hour after a sudden increase and expansion of the high-latitude convection and prompt penetration of the electric field to the equator associated with the southward shifting of IMF B_z. At present, GNSS is widely used to observe ionospheric disturbances caused by geomagnetic storms [*Ding et al.*, 2007; *Sharma et al.*, 2020; *Sori et al.*, 2019], earthquakes [*Liu et al.*, 2009; *Pulinets et al.*, 2005; *Sharma et al.*, 2017; *Tsugawa et al.*, 2018], and space weather events [*Ali et al.*, 2021; *Bergeot et al.*, 2013; *Fayose et al.*, 2012; *Ho et al.*, 1998] and can be used to monitor such phenomena by analyzing variations of ionospheric TEC.

Due to the influence of the ionosphere on radio signals, studies of ionosphere dynamics and disturbances during geomagnetic storms have great importance. In this paper, we present the study of the behavior of TEC during intense, moderate, and weak geomagnetic storms at four GPS stations of Nepal, located at different geographical latitudes and longitudes. These events are widely studied and provide good research cases for studying various ionospheric variations. The paper is organized as follows. In section 2, we describe data and measurement. In section 3, we present our results and discussion. Finally, we conclude our findings in section 4.

2. Data and measurements

In this work, we used an Internet-based supply of data provided by Operating Mission as Nodes on the Internet web system (OMNI). From the OMNI data explorer, we selected the data of velocity of solar wind flow (V_{sw}), plasma density (N_{sw}), plasma flow pressure (P_{sw}), the southward component of interplanetary magnetic field (IMF B_z), and geomagnetic indices, auroral electrojet (AE), the symmetric horizontal component of the geomagnetic field (SYM-H). These data are made readily available from the web page: https://omniweb.gsfc.nasa.gov/ow.html. For the selected date-time and geographical locations, TEC derived from ground-based dual-frequency GPS data was taken from UNAVCO (https://www.unavco.org/). The geographic coordinates of the stations are listed in Table 1, along with the geomagnetic activity. The network of GPS receiver stations used in this study in the map of Nepal is depicted in Figure 1. The dual-frequency radio signals of the Global Positing System (GPS) allow the monitoring of TEC along the ray path from the GPS satellite to the ground receiver [*Otsuka et al.*, 2002]. The TEC is measured in a unit called TECU, where 1 TECU = 10^{16} electrons/m^2. Ionospheric TEC is calculated using code-delay and carrier phase measurements recorded by ground-based GPS receivers. The TEC that we calculated from the accessible GPS RINEX data has been calibrated using the technique described in *Ciraolo et al.* [2007].

2.1. Detrended cross-correlation

Cross-correlation is the function of relative time between the signals, which compares an unknown signal with a known signal to determine similarities and draw relative characteristics that may reveal new information [*Usoro*, 2015]. Researchers [e.g., *Poudel et al.*, 2020; *Silwal et al.*, 2021b; *Vichare et al.*, 2012] have mentioned it as the standard tool for measuring statistical relation among various parameters. The correlation coefficient ranges from −1 to +1, where ±1 indicates a very strong correlation, and value near 0 indicates a weak correlation. To obtain insights into the mechanisms of natural processes, cross-correlation and autocorrelation functions, are often used; these approaches should only be used in the context of stationarity, as per their definitions [*Podobnik et al.*, 2009]. On the other hand, numerous time series of physical, biological, economic, and social systems are nonstationary and have long-range power-law associations; because of these

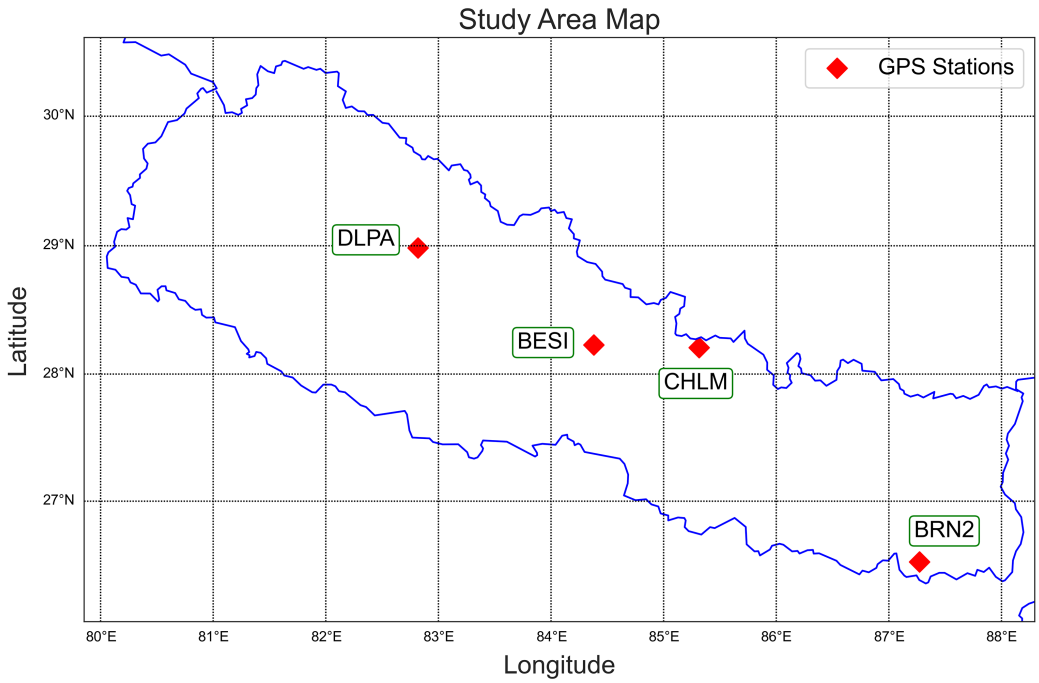

Figure 1. Map of Nepal showing the GPS receiver stations from which data was obtained.

non-stationarities, statistical features of these systems are harder to analyse in practice [*Podobnik et al.*, 2009]. In order to investigate the long-range cross-correlation involving non-stationarity, *Podobnik and Stanley* [2008] perfomed a revision of covariance analysis to introduce Detrended Cross-correlation Analysis (DXA). In this work, the DXA tool has been used to establish the relation of GPS-derived VTEC from ground-based monitoring receivers with different solar wind parameters and geomagnetic indices. The lead or lag between the indices was determined using the time scale. The detailed explanation and mathematical expressions of DXA can be found in the papers, *Podobnik and Stanley* [2008] and *Podobnik et al.* [2009].

Table 1. Information of events and stations for TEC measurements

Event Date	Geomagnetic Activity	Minimum *SYM-H* (nT)	GPS station	Geographic Latitude	Geographic Longitude
2017-08-04	Minor	−35	BESI	28.2286 °N	84.3797 °E
2017-07-16	Moderate	−67	DLPA	28.9837 °N	82.8179 °E
2017-09-08	Severe	−146	BRN2	26.5197 °N	87.2722 °E
			CHLM	28.2072 °N	85.3141 °E

3. Result and discussion

In this section, we have described the observations and results of three different events. The geomagnetic activities were classified as minor, moderate, and severe conditions. These classifications were done based on the geomagnetic index, *SYM-H*, which was first provided by *Kamide et al.* [1998]. The *SYM-H* index summarizes the stages during a geomagnetic storm. The onset of a geomagnetic storm involves a sudden positive increase in *SYM-H* value, termed as Sudden Storm Commencement (SSC). It is due to the shock wave created by the sudden increase in solar wind arriving on the Earth, which causes the sudden field increase [*Yokoyama and Kamide*, 1997]. Then, the elevated field does not change significantly for a certain period of time, referred to as the initial phase of the storm. When the enhanced solar stream reaches the Earth's magnetosphere, it increases

the number of energetic particles in the magnetosphere's trapping region, resulting in the increment of the ring current and hence causes the depression of *SYM-H* [*Gonzalez et al.*, 1999]. This depression in *SYM-H* is referred to as the main phase, which exists for one to a few hours. When new particles are no longer injected, the ring currents decay slowly for one or two days. The excess particles are lost during this time, and the magnetic field gradually returns to its normal value. This period is referred to as the recovery phase, which normally lasts for a few hours to days depending upon the strength and interplanetary origin of the geomagnetic storm. Since *SYM-H* has the distinct advantage of having 1-min time resolution compared to the 1-hour time resolution of *Dst*, we used *SYM-H* to identify the geomagnetic conditions based on the intensity of the storm time ring current. As the *Dst* index is calculated as an hourly index from the horizontal magnetic field component (*SYM-H*) at four magnetic observatories, *Dst* value with ($-50 < Dst \leq -30$ nT), ($-100 \leq Dst \leq -50$ nT) and ($-250 \leq Dst \leq -100$ nT), are categorized as minor, moderate and severe geomagnetic storms respectively [*Gonzalez et al.*, 1994]. We have compared the event day TEC with the mean TEC of the top five quietest days of the respective month for each event from four GPS stations and finally discussed the cross-correlation of VTEC with other solar wind parameters.

3.1. Observed geomagnetic indices and solar wind parameters

3.1.1. Event 1: 03 August to 05 August 2017

The indicative study presented in Figure 2 represents variation in interplanetary parameters and geomagnetic indices during a minor storm that occurred during 03–05 August 2017. This figure shows that the storm's first SSC occurred around 01:30 UT on 04 August, followed by the second SSC around 03:50 UT on the same day. *SYM-H* reached its minimum value of ∼ – 34 nT at 14:38 UT during the storm's main phase. Finally, the recovery phase started at 15:00 UT on the same day, which lasted for few days. One can observe that when the magnetosphere is under quiet conditions, the solar wind parameters and geomagnetic indices do not show significant fluctuations, as indicated by their observed value on the day before (03 August 2017) the main event. On the

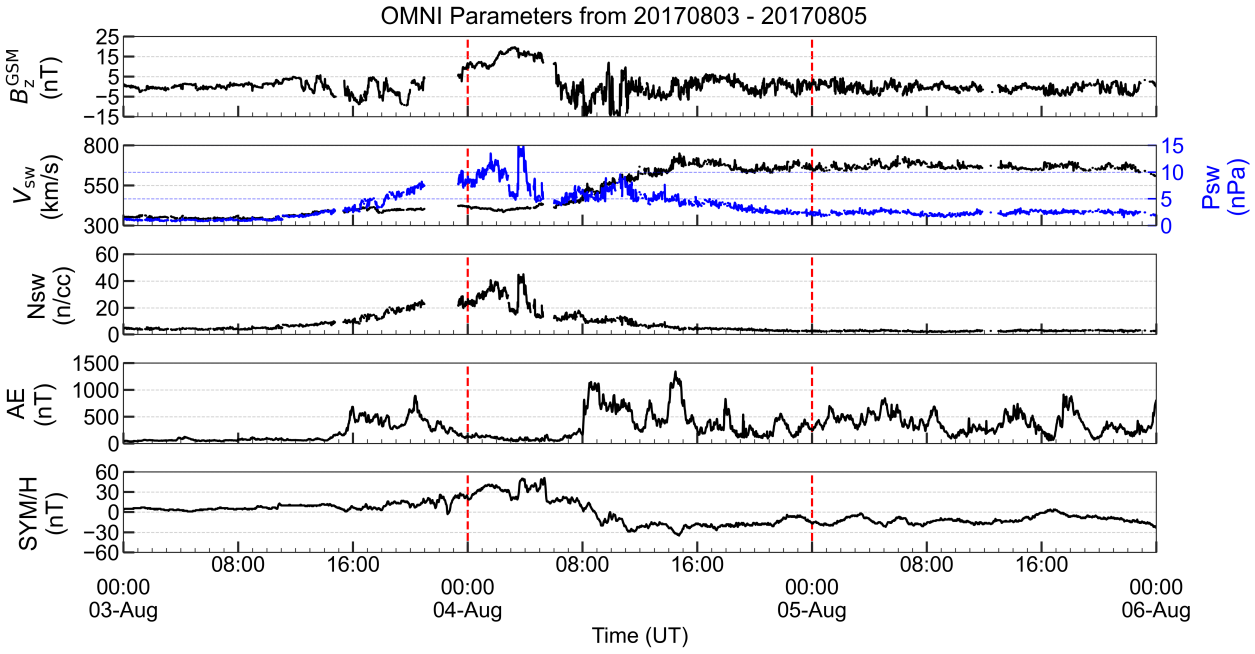

Figure 2. From top to bottom, the panels show the variation of the south-north component of Interplanetary magnetic field IMF B_z (nT) in GSM coordinate system, plasma flow speed V_{sw} (km/s) and solar wind dynamic pressure P_{sw} (nPa) (left), proton density N_{sw} (n/cc), *AE* (nT) and *SYM-H* (nT) index with time (UT) respectively during the geomagnetic storm of 03–05 August 2017.

contrary, under the development of the storm, IMF B_z started shifting southward, reaching a value of −6.51 nT and −15 nT at ∼06:31 UT and ∼10:30 UT, respectively, on 04 August. A strongly negative B_z causes magnetic reconnection between the interplanetary magnetic field (IMF) and the geomagnetic field to occur, resulting in the creation of open field lines, which allow mass, energy, and momentum to be transmitted from the solar wind to the Earth's magnetosphere [*Dungey*, 1961]. The plasma density climbed sharply to 45 n/cc around the initial phase of the storm at ∼03:50 UT and then gradually decreased. The flow speed (V_{sw}) shows a moderate speed stream of 400 km/s from 00:00 to 08:00 UT, and then it started increasing to attain a peak value of 750 km/s at ∼14:45 UT. Subsequently, a steady value of 600–700 km/s was maintained for the remaining period. One thing to be noted here was that the solar wind dynamic pressure (P_{sw}) arrived earlier before the event day. The plasma pressure started began to rise from 16:30 UT of 03 August. On 04 August, its value gradually increases to a peak of ∼15 nPa around 03:00 UT. In addition, one of the geomagnetic indices, the *AE* index, reached a value of >1000 nT at two time periods, one during 08:00–09:00 UT and the other during 14:00–15:00 UT. While the *AE* index value is tens of nT during a quiet period, it jumps to several hundred and more than a thousand nT during storms and substorms [*Rostoker*, 1972]. Thus, the observed values of solar wind parameters and geomagnetic indices characterized a minor condition of geomagnetic activity during this event. The minor events occur at an average of 1700 per cycle (1 cycle = 11 years), which can cause a minor impact on satellite operations (https://www.swpc.noaa.gov/NOAAscales).

3.1.2. Event 2: 15 July to 17 July 2017

Figure 3 represents the variation of the aforementioned interplanetary parameters and geomagnetic indices during a moderate geomagnetic storm on 15–17 July 2017. In this figure, the SSC occurred at 06:00 UT on 16 July as recognized in the *SYM-H* index (86 nT) of the bottom panel of Figure 3. Value of *SYM-H* reached −67 nT at its minimum around 15:30 UT during the main phase of the storm. At the onset of 16 July storm, the IMF B_z suddenly shifted northward to reach a value of 8 nT as seen in the first panel of Figure 3,

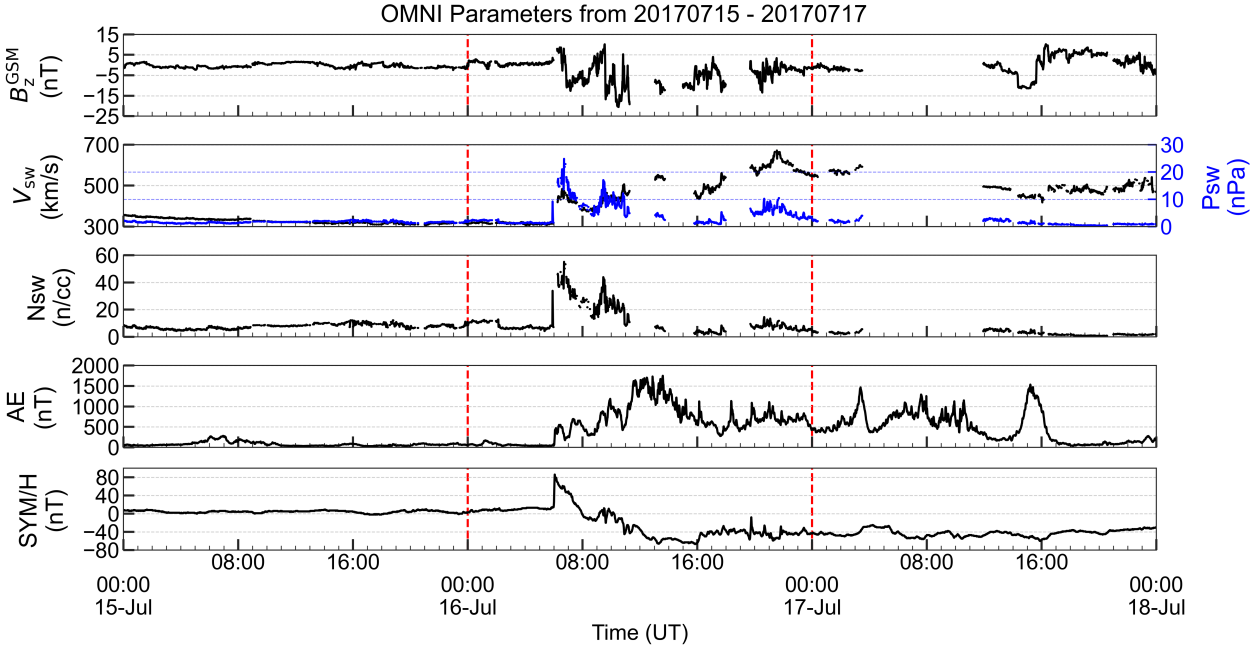

Figure 3. From top to bottom, the panels show the variation of the south-north component of Interplanetary magnetic field IMF B_z (nT) in GSM coordinate system, plasma flow speed V_{sw} (km/s) and solar wind dynamic pressure P_{sw} (nPa) (left), proton density N_{sw} (n/cc), *AE* (nT) and *SYM-H* (nT) index with time (UT) respectively during the geomagnetic storm of 15–17 July 2017.

then it dropped below a value of −10 nT at ~06:54 UT, and finally reached a minimum of −21 nT at 10:30 UT, and remained below −15 nT until 17:00 UT. The plasma density showed no fluctuation until 05:54 UT, but then it rapidly increased to a value of 55 n/cc at 06:43 UT. Meanwhile, the flow speed (V_{sw}) suddenly peaked from a moderate speed stream of < 400 km/s (00:00 to 06:35 UT) to > 400 km/s after 06:40 UT. The stream again peaked with a value of 671 km/s at ~21:33 UT. Subsequently, a steady value was maintained, and then it gradually decreased during the recovery phase of the storm. Also, the solar wind dynamic pressure (P_{sw}) had no effect on 15 July, but on 16 July, its value gradually increased to attain a maximum value of ~24 nPa at 06:43 UT. The abrupt variation of the solar wind parameters began around the SSC of the storm. Similarly, the *AE* index (second last panel of Figure 3) showed rapid variation right after the SSC. The *AE* index reached a peak value of >1500 nT during the storm's main phase. After that, *AE* recovers gradually, reaching a minimum value of <400 nT. During geomagnetic storm periods, the fluctuations in the IMF and solar wind velocity can initiate the substorms [*Nayar et al.*, 2006]. This is justified by the intensification of the *AE* index, which is a primary indicator of magnetospheric substorm activity [*Rostoker*, 1972; *Shadrina*, 2017]. In a cycle of 11 years, moderate events occur at an average of 600, fading HF radio propagation at higher latitudes (https://www.swpc.noaa.gov/NOAAscales).

3.1.3. Event 3: 07 September to 09 September 2017

Figure 4 represents the variation in interplanetary parameters and geomagnetic indices during geomagnetic storms that occurred on 07–09 September 2017. The September 2017 space weather events were studied widely because of the complex conditions for the solar and geomagnetic activity, coupled with several solar flares [e.g., *Clilverd et al.*, 2021; *Kumar and Kumar*, 2020; *Liu et al.*, 2019; *Yasyukevich et al.*, 2018] and storm-related activity that resulted in two consecutive *Dst* minima separated by approximately 13 hours on the same

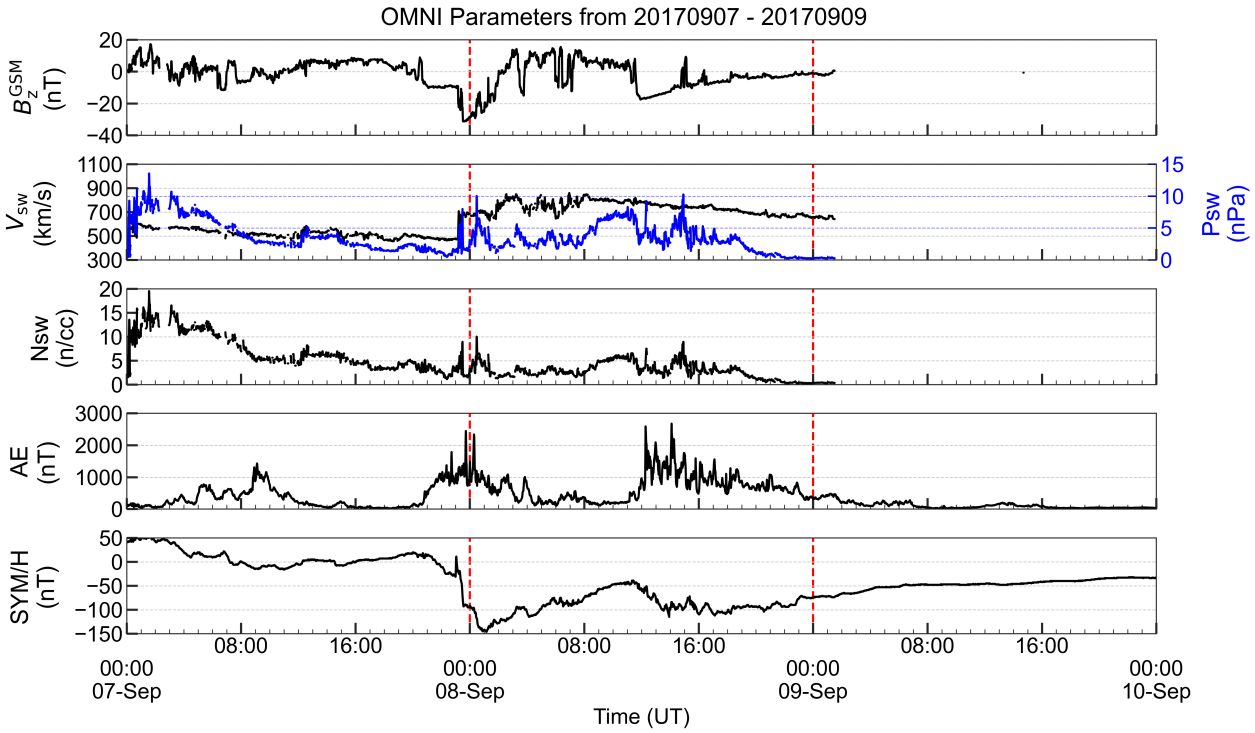

Figure 4. From top to bottom, the panels show the variation of the south-north component of Interplanetary magnetic field IMF B_z (nT) in GSM coordinate system, plasma flow speed V_{sw} (km/s) and solar wind dynamic pressure P_{sw} (nPa) (left), proton density N_{sw} (n/cc), *AE* (nT) and SYM/H (nT) index with time (UT) respectively during the geomagnetic storm of 07–09 September 2017.

day [*Blagoveshchensky et al.*, 2019; *Lei et al.*, 2018]. On 08 September 2017, an intense geomagnetic storm (G4) occurred with its first main phase at 01:00 UT, having a minimum *SYM-H* index of −146 nT and the second main phase during the first main phase recovery, having a minimum *SYM-H* index of −112 nT at 17:00 UT. The two minima peak values observed indicate a magnetic shock in the interplanetary medium [*Adebesin and Ikubanni*, 2011]. As depicted by Figure 4, the IMF B_z declined below a value of −30 nT at 23:30 UT on 07 September. It remained southward till 02:10 UT on 08 September and then turned northward–southward continuously until the second initial phase. As soon as the second initial phase started, it sharply turned southward to reach a value of −17 nT at 12:30 UT. Then after it slowly gained its normal value during the recovery phase of the storm. The plasma density (N_{sw}) reached a maximum value of 9 n/cc and 10 n/cc around 23:30 UT on 07 September and 00:00 UT on 08 September, which closely matched the time period of the initial and main phase of the storm, respectively. On 08 September, there was an inclining speed of plasma until a large forward shock arrives near 08:00 UT. The abrupt increase in speed from approximately 600 km/s to more than 800 km/s is a clear indication of this shock. An increase in the solar wind/magnetosphere coupling efficiency was projected instantly after an abrupt increase in solar wind dynamic pressure during steady southward IMF configuration [*Adebesin and Ikubanni*, 2011]. The solar wind dynamic pressure (P_{sw}) shows a good correlation with N_{sw} as indicated by the similar response to storm events, i.e., gradually increasing to its peak value of ~9 nPa and 10 nPa around 23:30 UT on 07 September and 00:00 UT on 08 September, respectively. Similarly, the *AE* index ranges from 0 to a peak value of >2000 nT around 23:30 UT (first initial phase), 00:30 UT (main phase), and 14:00 UT (second main phase) and then gradually recovers.

3.2. Observed TEC variation during geomagnetic activity

3.2.1. TEC response to the geomagnetic storm of 04 August 2017

Figure 5 shows the variation of TEC level during the minor storm of 04 August 2017 along with the mean TEC of the top five quietest days of the same month at BESI, BRN2, CHLM, and DLPA stations. Generally, the diurnal variation of TEC is minimum in

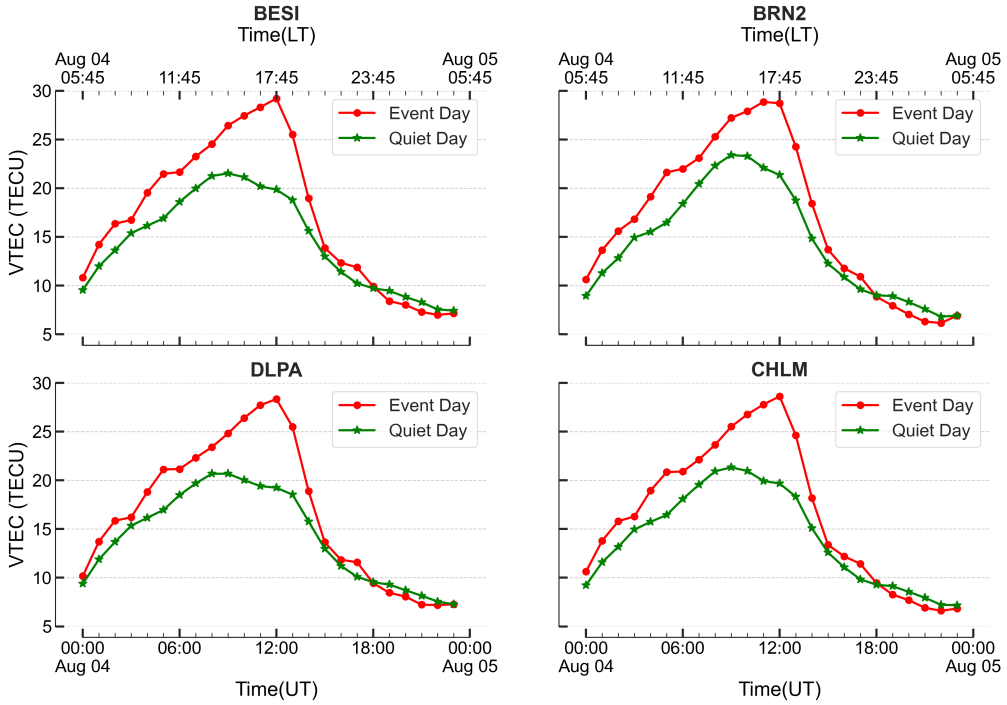

Figure 5. Comparison of TEC at four different stations during the minor storm of 04 August 2017 with the mean TEC of top five quietest days of the month.

a predawn, a continuous inclination in the early morning followed by an afternoon with maximum TEC value, and then gradually decreases after the sunset. In this study, the trend of diurnal variation of average VTEC seems to be followed. From Figure 5, it was found that the value of TEC was greater for a disturbed day in comparison to the quiet day's value over all stations. As it can be seen, the VTEC increment between the minor disturbed day and the quiet day was found to be around ~3–5 TECU. While the configuration and complexities of the equatorial ionosphere in the quiet period are governed primarily by electric fields, produced by the combination of the *E* and *F* dynamo processes, electrical field disturbances of magnetosphere origin are by far the most significant contributor to the equatorial ionosphere storm response [*Fejer*, 2003; *Fejer et al.*, 1995]. The disturbed electric fields can cause the ionospheric plasma to be redistributed and result in significant variations in TEC over the path of radio signals transmission [*Sreeja et al.*, 2009; *Tsurutani et al.*, 2004].

3.2.2. TEC response to the geomagnetic storm of 16 July 2017

Similarly, Figure 6 shows the variation of TEC during the moderate storm of 16 July 2017 along with the mean TEC of the top five quietest days of the same month from four GPS stations. One can observe that both disturbed day and quiet day followed the diurnal pattern of VTEC in case of a moderate storm event. It was also found that the value of TEC was quite similar in the morning time during 00:00–08:00 UT in both quiet day and disturbed day, as indicated by a very low differential TEC value (<1 TECU), but later on, the TEC value gradually increases and attained a maximum value around 12:00 UT, corresponding to the difference of >5 TECU at all four stations. Then, it started decreasing continuously and then suddenly peaked at ~17:00 UT. The post-sunset increase in TEC could be related to the post-sunset increase in the upward $\mathbf{E} \times \mathbf{B}$ drift velocity [*Anderson and Klobuchar*, 1983]. The VTEC then gradually returns to the normal value with the recovery phase of the storm.

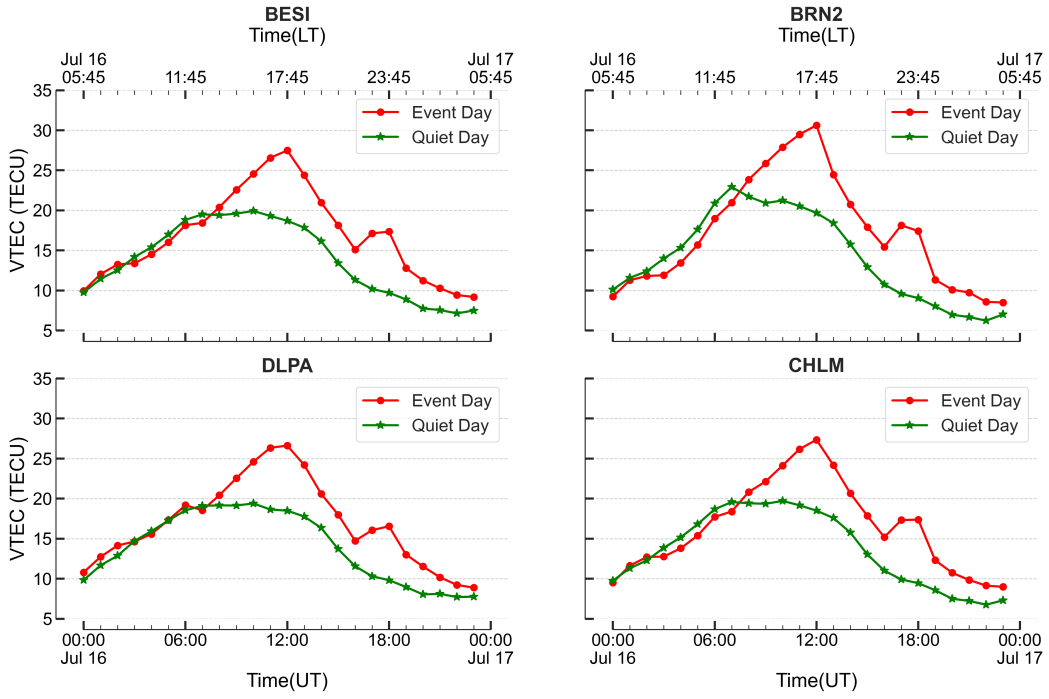

Figure 6. Comparison of TEC at four different stations during the moderate storm of 16 July 2017 with the mean TEC of most five quietest days of the month.

3.2.3. TEC response to the geomagnetic storm of 08 September 2017

Figure 7 shows the variation of the TEC during the intense storm of 08 September 2017, along with the mean TEC of the top five quietest days of the same month. This figure reveals a considerable increase in the VTEC value during the storm when comparing a storm day to a quiet day. During a severe geomagnetic storm, the diurnal variation pattern of the minimum VTEC in the predawn hours was not followed. This could have occurred due to the onset time of the storm as the initial phase of the storm occurred during the nighttime around 23:30 UT on 07 September [*Bhattarai et al.*, 2016]. In addition, this is mainly owing to the combined influence of prompt penetrating electric fields (PPEFs) associated with the prolonged duration of southern shifting of second main phase IMF B_z and first main phase disturbance dynamo electric fields (DDEFs) [*Berdermann et al.*, 2018; *Li et al.*, 2018]. A very high VTEC value in comparison to the aforementioned geomagnetic events endured throughout the entire time period of 08 September. One of the noteworthy findings was the multistep VTEC variation on the severe geomagnetic event, i.e., it first sharply increased during 00:00–03:00 UT, then it suddenly decreased at 04:00 UT and again started increasing to attain a peak value of 40 TECU, 38 TECU, 43 TECU and 40 TECU at CHLM, DLPA, BRN2, and BESI stations, respectively, exactly at the same time, 06:00 UT. Then, it gradually decreased for the remaining time period. In addition, we noticed a slight increase in the VTEC value around 14:00 UT. It could be related to the second initial phase of the storm that occurred at 14:00 UT. As a whole, the VTEC enhancements were attributed to the combined impacts of PPEFs and suddenly increased extreme ultraviolet (EUV) radiations and X-rays accompanied with the solar flare [*Kumar and Kumar*, 2020].

3.3. Deviation of TEC during storm day over quiet day

It is known that the TEC value changes as a function of geographic latitude and longitude, and local time because these parameters impact the electron density distribution in the ionosphere. Because of this, in order to analyze the components of the TEC value that are modified during geomagnetic storms, we must subtract the background TEC value

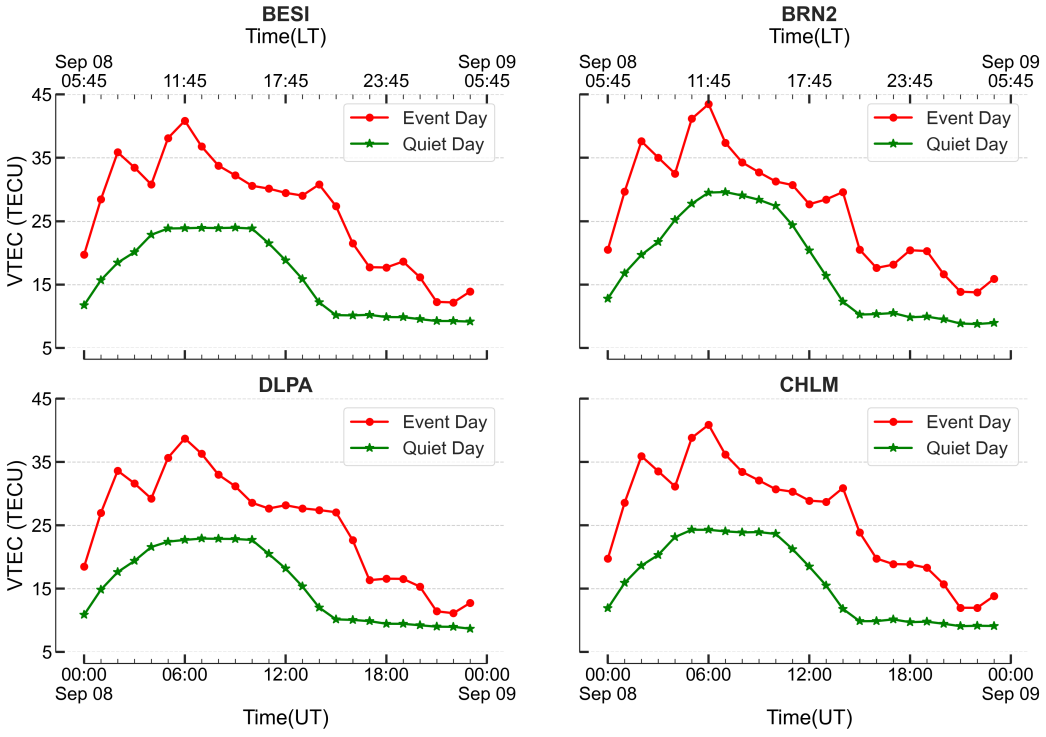

Figure 7. Comparison of TEC at four different stations during the intense storm of 08 September 2017 with the mean TEC of most five quietest days of the month.

obtained during geomagnetically quiet conditions from the observed TEC value [*Immel and Mannucci*, 2013]. We first calculated the average VTEC value of five geomagnetically quiet days of the month and then subtracted it from the VTEC value of the storm day, which we termed as the deviation in VTEC (dVTEC).

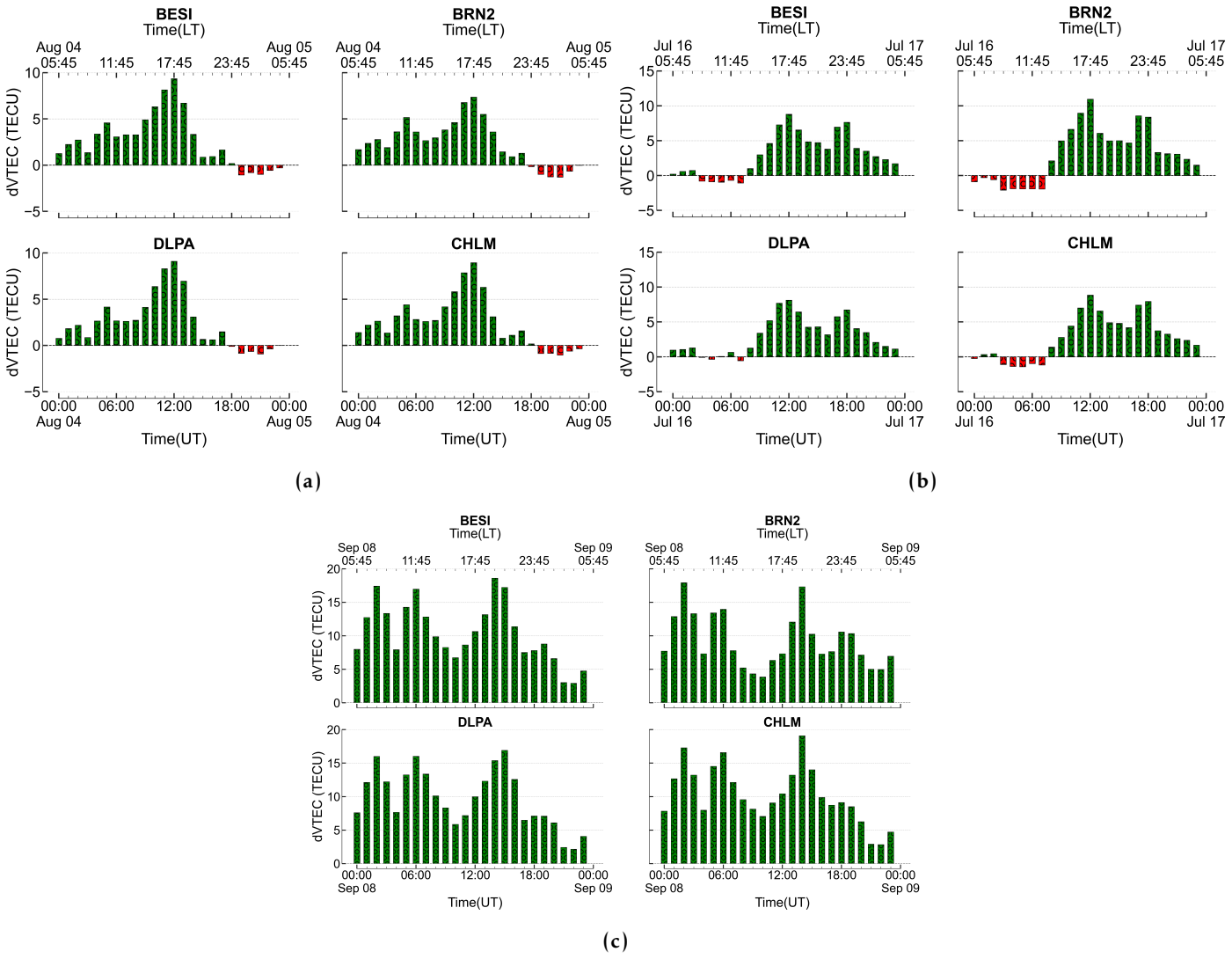

Figure 8. Deviation in VTEC (negative for depletion or positive for enhancement) (dVTEC) charts at four different GPS stations BESI, CHLM, BRN2, and DLPA, during event days 04 August 2017 (a), 16 July 2017 (b), and 08 September 2017 (c).

The deviation of VTEC during three geomagnetically disturbed days is shown in Figure 8. Figure 8a represents the deviation in VTEC on a minor event day, i.e., 04 August 2017, where the maximum deviation value of VTEC was found to be ~7–9 TECU. Similarly, the maximum dVTEC was observed in the range of 8 TECU to 12 TECU on 16 July 2017, with some negative deviation in morning hours, as seen in Figure 8b. Finally, Figure 8c depicted that the highest dVTEC was recorded in the intense geomagnetic event within the range of 2–15 TECU, and in some hours of UT, it exceeded more than 18 TECU compared to that of quiet days. Also, no negative deviation in VTEC was seen throughout this event, which can have significant effects on radio communications and navigation systems [*Mendillo*, 2006]. Similarly, *Akintufede et al.* [2017], *Bhattarai et al.* [2016], and *Jain et al.* [2010] had also mentioned an increment or decrement in TEC value with the strength of geomagnetic storms under positive or negative storm effect, respectively, at low latitude stations. These previous works strongly support our findings.

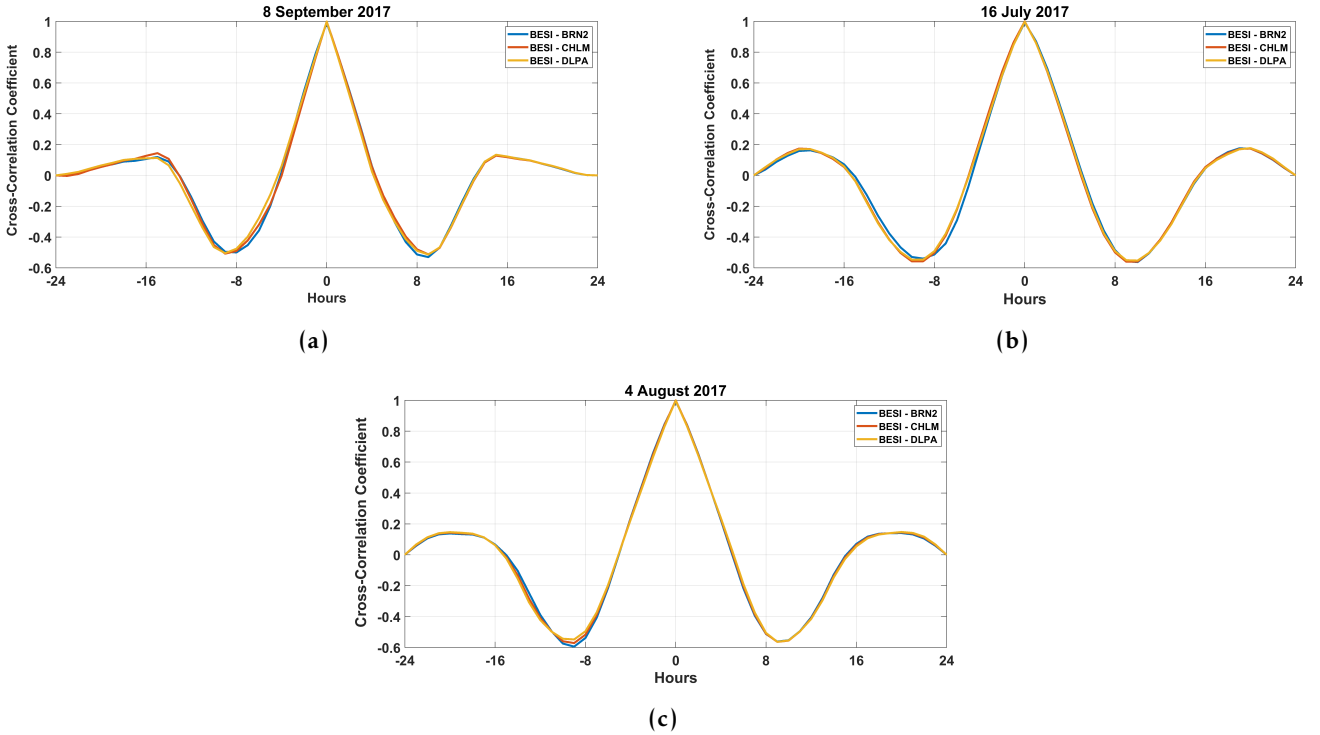

Figure 9. Cross-correlation of mean hourly VTEC data obtained from BESI GPS station with VTEC data from BRN2, CHLM, and DLPA GPS stations on 08 September 2017 (a), 16 July 2017 (b), and 04 August 2017 (c).

3.4. DXA analysis

Figure 9a, Figure 9b, and Figure 9c show the plot of cross-correlation of mean hourly VTEC derived from BESI GPS station with mean hourly VTEC extracted from BRN2, CHLM, and DLPA GPS stations during the geomagnetic event of 08 September, 16 July and 04 August of the year 2017, respectively. The horizontal axis represents the time scale in hours ranging from −24 to 24, and the vertical axis represents the cross-correlation coefficient. Time scales are used to determine the lead or lag between the indices after establishing their correlation [*Bhattarai et al.*, 2016; *Poudel et al.*, 2020]. Figures portrayed the cross-correlation coefficient of +0.98 at a zero-time lag, revealing the strong positive correlation of mean hourly VTEC computed from BESI GPS station with other studied stations in all events. More detailed information on the correlation coefficients with corresponding lead/lag can be obtained from Table 2. Thus, the response of VTEC over Nepal regions towards three different geomagnetic events was relatively the same. This result facilitates us to select the BESI GPS station as a reference station and has been used to represent all other stations for studying the relationship of VTEC with interplanetary parameters and geomagnetic indices.

Table 2. Cross-correlation coefficients and time lead/lag of VTEC at different stations during geomagnetic storm events

Correlating Parameters (VTEC)	4 August 2017		16 July 2017		8 September 2017	
	Coeff.	Lead (+) /Lag (−) (hrs)	Coeff.	Lead (+)/ Lag (−) (hrs)	Coeff.	Lead (+)/ Lag (−) (hrs)
BESI-BRN2	+0.98	0	+0.98	0	+0.98	0
BESI-CHLM	+0.98	0	+0.98	0	+0.98	0
BESI-DLPA	+0.98	0	+0.98	0	+0.98	0

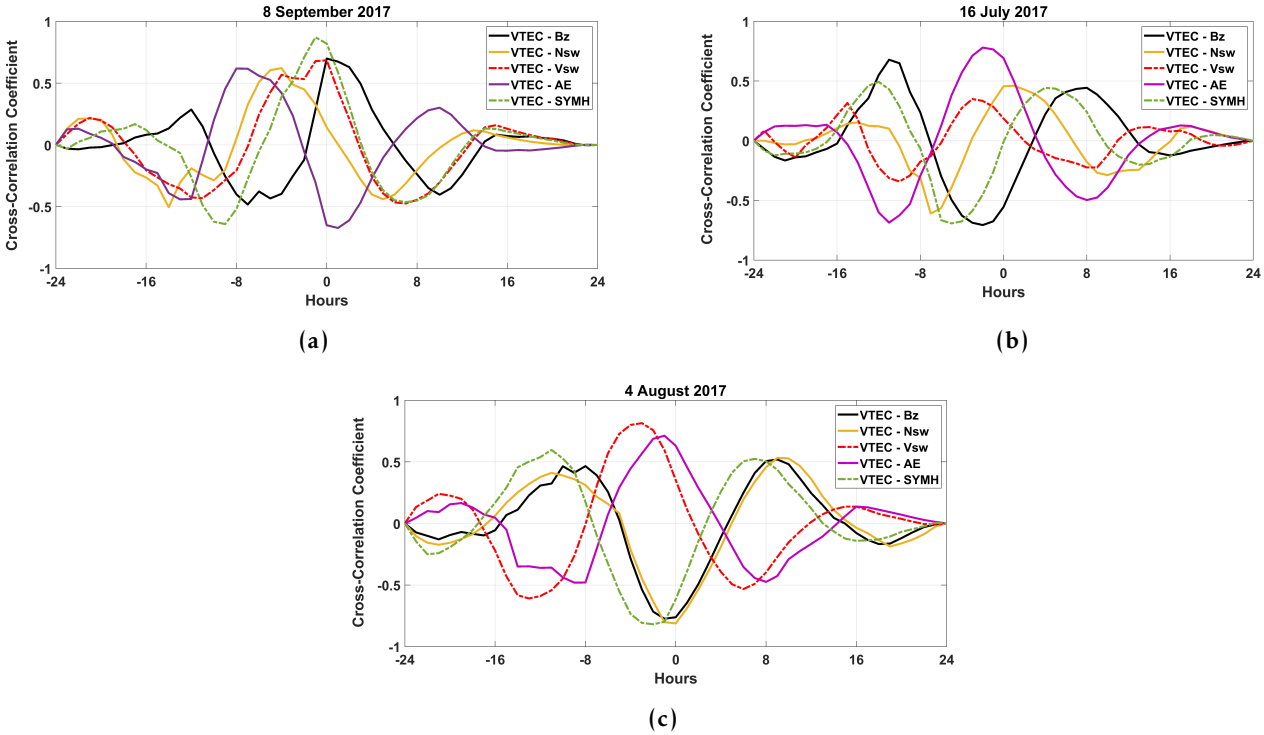

Figure 10. Cross-correlation of GPS-VTEC with the component of Interplanetary magnetic field IMF B_z (nT) in GSM coordinate system, plasma density N_{sw} (n/cc), flow speed V_{sw} (km/s), *AE* (nT), and symmetric horizontal component of geomagnetic field *SYM-H* (nT) on 08 September 2017 (a), 16 July 2017 (b) and 04 August 2017 (c).

Figure 10a depicts the cross-correlation of VTEC with IMF B_z, N_{sw}, V_{sw}, *AE*, and *SYM-H* during severe geomagnetic storm day, which occurred on 08 September 2017. The figure showed the positive correlation of VTEC with B_z (black curve) and V_{sw} (red curve) having cross-correlation coefficients of +0.69 and +0.68, respectively, at zero-time lag. Similarly, N_{sw} (yellow curve) and *SYM-H* (green curve) correlated positively with VTEC showing a maximum correlation coefficient of +0.62 and +0.87, but at a time lag of −4 and −1 hrs. This result reveals that the VTEC lags N_{sw} and *SYM-H* by 4 and 1 hrs, respectively, before being correlated [*Adhikari et al.*, 2018]. However, VTEC showed a negative correlation with *AE* (purple curve) during severe storm days. On this day, the VTEC-*AE* curve peaked with a correlation coefficient of −0.67 at +1 hrs time lag, manifesting the inverse relation of *AE* and VTEC. The cross-correlation plot during the moderate geomagnetic storm that occurred on 16 July 2017 is represented in Figure 10b. In the figure, the red and purple curve indicated a positive correlation of VTEC with V_{sw} and *AE*, attaining a peak cross-correlation coefficient of +0.35 and +0.78 at the time lag of −3 and −2 hrs, respectively. This shows that the VTEC is moderately correlated with the solar wind speed for a moderate storm. Also, the VTEC exhibited an inverse relation with B_z, N_{sw} and *SYM-H* with corresponding correlation coefficient of −0.70, −0.61 and −0.69 at the time lag of −2, −7 and −5 hrs, respectively. However, the same parameters were correlated positively with VTEC in the severe storm event. This shows the discrepancy in the correlation of VTEC with solar wind parameters at different events. Figure 10c shows the cross-correlation of VTEC with the solar wind parameters during the minor geomagnetic storm on 04 August 2017. It exhibits a trend closely resembling that observed during the moderate storm with slightly improved cross-correlation coefficent. More detailed information on the correlation coefficients and the corresponding lead/lag time for all three events can be obtained from Table 3. Furthermore, it is important to note that the observed differences in time lag and correlation may arise from variations in the intensity and interplanetary origin of geomagnetic storms. Therefore, additional statistical analyses

of various such events are imperative to better understand the relationship between VTEC, solar wind parameters, and geomagnetic indices, ultimately enhancing our understanding of the ionosphere's response to these phenomena.

Table 3. Cross-correlation coefficients and time lead/lag of VTEC with solar wind parameters and geomagnetic indices during different geomagnetic storm events

Correlating Parameters (VTEC)	4 August 2017		16 July 2017		8 September 2017	
	Coeff.	Lead (+) /Lag (−) (hrs)	Coeff.	Lead (+)/ Lag (−) (hrs)	Coeff.	Lead (+) / Lag (−) (hrs)
VTEC – B_z	−0.79	−1	−0.70	−2	+0.69	0
VTEC – N_{sw}	−0.81	0	−0.61	−7	+0.62	−4
VTEC – V_{sw}	+0.81	−3	+0.35	−3	+0.68	0
VTEC – *AE*	+0.71	−1	+0.78	−2	−0.67	+1
VTEC – *SYM-H*	−0.82	−2	−0.69	−5	+0.87	−1

4. Conclusion

We presented a detailed study on the behavior of GPS-derived VTEC during three different geomagnetically disturbed days. In order to classify the disturbed days from minor to severe, we analyzed the different geomagnetic indices (*AE* index and *SYM-H* index) and solar wind parameters (V_{sw}, IMF B_z, N_{sw} and P_{sw}). The variation on mean hourly VTEC on these geomagnetically disturbed days was studied by comparing it with mean hourly GPS-derived VTEC on quiet days of respective event month. Moreover, we used the cross-correlation analysis of mean hourly VTEC data with several interplanetary and geomagnetic parameters. Besides, the similarity pattern of the VTEC variation at the mentioned GPS stations with each other was also studied using the cross-correlation approach. The results of this study can be summarised as follows:

1. The diurnal variation pattern of VTEC was preserved in a minor and moderate storm day, i.e., minimum VTEC value during the predawn and morning hours, reach maximum during day hours, and again decrease during night hours. A similar pattern was followed in quiet days but with low VTEC values. However, in the case of a severe geomagnetic storm, we noticed an unusual diurnal pattern during the predawn, which might have occurred due to the development of the geomagnetic storm in the late nights' hours of the day before the main event.
2. The VTEC enhancement was significantly high on the severely disturbed day, followed by the moderate storm and the minor storm. Ultimately, the deviation of GPS-derived VTEC on event days from quiet day value was maximum during a severe geomagnetic storm day, compared to the moderate and minor event day.
3. Cross-correlation analysis presented the association of VTEC value with solar wind parameters and geomagnetic indices. During all three event days, the VTEC value shows a positive association with solar wind velocity only. During minor and moderate storm events, the solar wind parameters (IMF B_z, N_{sw}) and the geomagnetic index (*SYM-H*) exhibit negative correlation with VTEC, showing relatively short time lags. In contrast, during severe storms, these parameters show positive correlations with time lags in the range of −1 to +1 hr. In addition, our results revealed that VTEC and *AE* index has a good positive association in minor and moderate storm events and a moderate negative correlation in severe storm event. Thus, it is not advisable to rely on only one interplanetary or geomagnetic parameter in a study of individual events, particularly where one is interested to track the variation characteristics of VTEC during geomagnetic activity.
4. The result observed from the cross-correlation of hourly mean VTEC value of BESI GPS station with other stations presented a good association of VTEC data between

different GPS stations of Nepal in all types of storm events. This suggests that the ionospheric response to the geomagnetic storms across different stations in Nepal is quite similar. Further, the DXA method has proven to be effective in examining the relationship between two time series data characterized by non-stationarity.

5. Observing and analyzing ionospheric perturbations over Nepal during geomagnetic storms demonstrated that the GPS measurement of ionospheric TEC appears to be quite effective in monitoring space weather activities.

It is essential to conduct these sorts of studies over EIA regions because the equatorial plasma fountain is particularly sensitive to disturbance electric fields. Combining measurements from various geomagnetic storms can mitigate disturbances associated with radio signal propagation, power grid fluctuations, and widespread voltage control problems in power systems, induced pipeline currents, and satellite orientation problems by monitoring solar activities and the ionospheric response during multiple space weather events. In the future, we can investigate the long-term data set of TEC and electron density profiles from satellite measurements and conduct a comparative analysis using ground- and space-based observations from various regions, which will enable us to study the mechanisms underlying ionospheric changes better than ever before. Ultimately, this study would serve as a baseline for providing crucial information on ionospheric variability, and future researchers can use these data to improve models of ionospheric dynamics.

Acknowledgments. GPS-derived TEC Data used for this study is obtained from the UNAVCO (https://www.unavco.org/), and the data of interplanetary parameters and geomagnetic indices are extracted from NASA websites (http://omniweb.gsfc.nasa.gov/ow_min.html). We want to thank staff members of NASA and UNAVCO for making the data publicly available. This study was conducted under self-funding.

References

Abdu, M. A. (2005), Equatorial ionosphere–thermosphere system: Electrodynamics and irregularities, *Advances in Space Research*, *35*(5), 771–787, https://doi.org/10.1016/j.asr.2005.03.150.

Abdu, M. A., J. W. MacDougall, I. S. Batista, J. H. A. Sobral, and P. T. Jayachandran (2003), Equatorial evening prereversal electric field enhancement and sporadic E layer disruption: A manifestation of E and F region coupling, *Journal of Geophysical Research*, *108*(A6), 1–13, https://doi.org/10.1029/2002JA009285.

Adebesin, B. O., and S. O. Ikubanni (2011), An Empirical Study into the Plasma Flow Speed Geoeffectiveness during different Geomagnetic Activities, *Continental Journal Applied Sciences*, *6*(3), 62–70.

Adhikari, B., S. Dahal, N. Sapkota, P. Baruwal, B. Bhattarai, K. Khanal, and N. P. Chapagain (2018), Field-aligned current and polar cap potential and geomagnetic disturbances: A review of cross-correlation analysis, *Earth and Space Science*, *5*(9), 440–455, https://doi.org/10.1029/2018EA000392.

Adhikari, B., B. Kaphle, N. Adhikari, S. Limbu, A. Sunar, R. K. Mishra, and S. Adhikari (2019), Analysis of cosmic ray, solar wind energies, components of Earth's magnetic field, and ionospheric total electron content during solar superstorm of November 18–22, 2003, *SN Applied Sciences*, *1*(5), 1–6, https://doi.org/10.1007/s42452-019-0474-8.

Akintufede, E., L. Olatunbosun, A. Olabode, A. Babinisi, and E. Ariyibi (2017), Total Electron Content Variations during Different Geomagnetic Activities in Ile-Ife, Nigeria, *Canadian Journal of Pure and Applied Sciences*, *11*(1), 4141–4149.

Ali, O. H., N. Zaourar, R. Fleury, and C. Amory-Mazaudier (2021), Transient variations of vertical total electron content at low latitude during the period 2013–2017, *Advances in Space Research*, *68*(12), 4857–4871, https://doi.org/10.1016/j.asr.2021.02.039.

Anderson, D. N., and J. A. Klobuchar (1983), Modeling the total electron content observations above Ascension Island, *Journal of Geophysical Research*, *88*(A10), 8020–8024, https://doi.org/10.1029/JA088iA10p08020.

Berdermann, J., M. Kriegel, D. Banyś, F. Heymann, M. M. Hoque, V. Wilken, C. Borries, A. Heßelbarth, and N. Jakowski (2018), Ionospheric response to the X9.3 flare on 6 September 2017 and its implication for navigation services over Europe, *Space Weather*, *16*(10), 1604–1615, https://doi.org/10.1029/2018sw001933.

Bergeot, N., I. Tsagouri, C. Bruyninx, J. Legrand, J.-M. Chevalier, P. Defraigne, Q. Baire, and E. Pottiaux (2013), The influence of space weather on ionospheric total electron content during the 23rd solar cycle, *Journal of Space Weather and Space Climate*, *3*, A25, https://doi.org/10.1051/swsc/2013047.

Bhattarai, N., N. P. Chapagain, and B. Adhikari (2016), Total Electron Content and Electron Density Profile Observations during Geomagnetic Storms using COSMIC Satellite Data, *Discovery*, *52*(250), 1979–1990.

Blagoveshchensky, D. V., M. A. Sergeeva, and P. Corona-Romero (2019), Features of the magnetic disturbance on September 7–8, 2017 by geophysical data, *Advances in Space Research*, *64*(1), 171–182, https://doi.org/10.1016/j.asr.2019.03.037.

Chapagain, N. P. (2016), Equatorial ionospheric plasma drifts velocities using radar observations, *BIBECHANA*, *14*, 1–8, https://doi.org/10.3126/bibechana.v14i0.15405.

Ciraolo, L., F. Azpilicueta, C. Brunini, A. Meza, and S. M. Radicella (2007), Calibration errors on experimental slant total electron content (TEC) determined with GPS, *Journal of Geodesy*, *81*(2), 111–120, https://doi.org/10.1007/s00190-006-0093-1.

Clilverd, M. A., C. J. Rodger, M. P. Freeman, J. B. Brundell, D. H. M. Manus, M. Dalzell, E. Clarke, A. W. P. Thomson, G. S. Richardson, F. MacLeod, and I. Frame (2021), Geomagnetically induced currents during the 07–08 September 2017 disturbed period: a global perspective, *Journal of Space Weather and Space Climate*, *11*, 33, https://doi.org/10.1051/swsc/2021014.

Danilov, A. D. (2001), F2-region response to geomagnetic disturbances, *Journal of Atmospheric and Solar-Terrestrial Physics*, *63*(5), 441–449, https://doi.org/10.1016/s1364-6826(00)00175-9.

Davies, K. (1990), *Ionospheric Radio*, 600 pp., Institution of Engineering and Technology, https://doi.org/10.1049/pbew031e.

de Abreu, A. J., I. M. Martin, P. R. Fagundes, K. Venkatesh, I. S. Batista, R. de Jesus, M. Rockenback, A. Coster, M. Gende, M. A. Alves, and M. Wild (2017), Ionospheric F-region observations over American sector during an intense space weather event using multi-instruments, *Journal of Atmospheric and Solar-Terrestrial Physics*, *156*, 1–14, https://doi.org/10.1016/j.jastp.2017.02.009.

de Gonzalez, A. L. C., A. M. da Costa, and W. D. Gonzalez (2004), Ring current space-time inhomogeneities in intense geomagnetic storms, *Geofisica Internacional*, *43*(2), 205–215, https://doi.org/10.22201/igeof.00167169p.2004.43.2.172.

Ding, F., W. Wan, B. Ning, and M. Wang (2007), Large-scale traveling ionospheric disturbances observed by GPS total electron content during the magnetic storm of 29–30 October 2003, *Journal of Geophysical Research: Space Physics*, *112*(A6), 1–15, https://doi.org/10.1029/2006ja012013.

Dungey, J. W. (1961), Interplanetary magnetic field and the auroral zones, *Physical Review Letters*, *6*(2), 47–48, https://doi.org/10.1103/PhysRevLett.6.47.

Fayose, R. S., R. Babatunde, O. Oladosu, and K. Groves (2012), Variation of Total Electron Content TEC and their effect on GNSS over Akure, Nigeria, *Applied Physics Research*, *4*(2), 105–109, https://doi.org/10.5539/apr.v4n2p105.

Fejer, B. G. (2003), Low-latitude ionospheric disturbance electric field effects during the recovery phase of the 19-21 October 1998 magnetic storm, *Journal of Geophysical Research*, *108*(A12), 1–10, https://doi.org/10.1029/2003ja010190.

Fejer, B. G., E. R. de Paula, R. A. Heelis, and W. B. Hanson (1995), Global equatorial ionospheric vertical plasma drifts measured by the AE-E satellite, *Journal of Geophysical Research*, *100*(A4), 5769–5776, https://doi.org/10.1029/94ja03240.

Fuller-Rowell, T. J., M. V. Codrescu, R. J. Moffett, and S. Quegan (1994), Response of the thermosphere and ionosphere to geomagnetic storms, *Journal of Geophysical Research*, *99*(A3), 3893–3914, https://doi.org/10.1029/93JA02015.

Gonzalez, W. D., J. A. Joselyn, Y. Kamide, H. W. Kroehl, G. Rostoker, B. T. Tsurutani, and V. M. Vasyliunas (1994), What is a geomagnetic storm?, *Journal of Geophysical Research*, *99*(A4), 5771–5792, https://doi.org/10.1029/93ja02867.

Gonzalez, W. D., B. T. Tsurutani, and A. L. C. de Gonzalez (1999), Interplanetary origin of geomagnetic storms, *Space Science Reviews*, *88*(3/4), 529–562, https://doi.org/10.1023/a:1005160129098.

Ho, C. M., A. J. Mannucci, L. Sparks, X. Pi, U. J. Lindqwister, B. D. Wilson, B. A. Iijima, and M. J. Reyes (1998), Ionospheric total electron content perturbations monitored by the GPS global network during two northern hemisphere winter storms, *Journal of Geophysical Research: Space Physics*, *103*(A11), 26,409–26,420, https://doi.org/10.1029/98ja01237.

Hofmann-Wellenhof, B., H. Lichtenegger, and J. Collins (2012), *Global positioning system: Theory and practice*, 382 pp., Springer Vienna, https://doi.org/10.1007/978-3-7091-6199-9.

Hu, T., Y. Yao, and J. Kong (2021), Study of Spatial and Temporal Variations of Ionospheric Total Electron Content in Japan, during 2014–2019 and the 2016 Kumamoto Earthquake, *Sensors*, *21*(6), 2156, https://doi.org/10.3390/s21062156.

Ikubanni, S. O., S. J. Adebiyi, B. O. Adebesin, and K. O. Dopamu (2018), Response of GPS-Tec in the African Equatorial Region to the Two Recent St. Patrick's Day Storms, *International Journal of Civil Engineering and Technology*, *9*(10), 1773–1790.

Immel, T. J., and A. J. Mannucci (2013), Ionospheric redistribution during geomagnetic storms, *Journal of Geophysical Research: Space Physics*, *118*(12), 7928–7939, https://doi.org/10.1002/2013ja018919.

Jain, A., S. Tiwari, S. Jain, and A. K. Gwal (2010), TEC response during severe geomagnetic storms near the crest of equatorial ionization anomaly, *Indian Journal of Radio & Space Physics*, *39*, 11–24.

Jankovičová, D., P. Dolinský, F. Valach, and Z. Vörös (2002), Neural network-based nonlinear prediction of magnetic storms, *Journal of Atmospheric and Solar-Terrestrial Physics*, *64*(5-6), 651–656, https://doi.org/10.1016/s1364-6826(02)00025-1.

Kamide, Y., W. Baumjohann, I. A. Daglis, W. D. Gonzalez, M. Grande, J. A. Joselyn, R. L. McPherron, J. L. Phillips, E. G. D. Reeves, G. Rostoker, A. S. Sharma, H. J. Singer, B. T. Tsurutani, and V. M. Vasyliunas (1998), Current understanding of magnetic storms: Storm-substorm relationships, *Journal of Geophysical Research: Space Physics*, *103*(A8), 17,705–17,728, https://doi.org/10.1029/98ja01426.

Kelly, M. C., M. N. Vlasov, J. C. Foster, and A. J. Coster (2004), A quantitative explanation for the phenomenon known as storm-enhanced density, *Geophysical Research Letters*, *31*(19), 1–3, https://doi.org/10.1029/2004gl020875.

Krypiak-Gregorczyk, A. (2018), Ionosphere response to three extreme events occurring near spring equinox in 2012, 2013 and 2015, observed by regional GNSS-TEC model, *Journal of Geodesy*, *93*(7), 931–951, https://doi.org/10.1007/s00190-018-1216-1.

Kumar, S., and S. Kumar (2020), Equatorial ionospheric TEC and scintillations under the space weather events of 4–9 September 2017: M-class solar flares and a G4 geomagnetic storm, *Journal of Atmospheric and Solar-Terrestrial Physics*, *209*, 105,421, https://doi.org/10.1016/j.jastp.2020.105421.

Lei, J., F. Huang, X. Chen, J. Zhong, D. Ren, W. Wang, X. Yue, X. Luan, M. Jia, X. Dou, L. Hu, B. Ning, C. Owolabi, J. Chen, G. Li, and X. Xue (2018), Was magnetic storm the only driver of the long-duration enhancements of daytime total electron content in the Asian-Australian sector between 7 and 12 September 2017?, *Journal of Geophysical Research: Space Physics*, *123*(4), 3217–3232, https://doi.org/10.1029/2017ja025166.

Li, W., J. Yue, Y. Yang, C. He, A. Hu, and K. Zhang (2018), Ionospheric and thermospheric responses to the recent strong solar flares on 6 September 2017, *Journal of Geophysical Research: Space Physics*, *123*(10), 8865–8883, https://doi.org/10.1029/2018ja025700.

Liu, J. Y., Y. I. Chen, C. H. Chen, C. Y. Liu, C. Y. Chen, M. Nishihashi, J. Z. Li, Y. Q. Xia, K. I. Oyama, K. Hattori, and C. H. Lin (2009), Seimo-ionospheric GPS total electron content anomalies observed before the 12 May 2008 Mw7. 9 Wenchuan earthquake, *Journal of Geophysical Research: Space Physics*, *114*(A4), 1–10, https://doi.org/10.1029/2008ja013698.

Liu, Y., Z. Li, L. Fu, J. Wang, and C. Zhang (2019), Studying the ionospheric responses induced by a geomagnetic storm in September 2017 with multiple observations in America, *GPS Solutions*, *24*(1), 1–13, https://doi.org/10.1007/s10291-019-0916-1.

Mansilla, G. A. (2019), Behavior of total electron content over the Arctic and Antarctic sectors during several intense geomagnetic storms, *Geodesy and Geodynamics*, *10*(1), 26–36, https://doi.org/10.1016/j.geog.2019.01.004.

Mendes, O., M. O. Domingues, A. M. da Costa, and A. L. C. de Gonzalez (2005), Wavelet analysis applied to magnetograms: Singularity detections related to geomagnetic storms, *Journal of Atmospheric and Solar-Terrestrial Physics*, *67*(17–18), 1827–1836, https://doi.org/10.1016/j.jastp.2005.07.004.

Mendillo, M. (2006), Storms in the ionosphere: Patterns and processes for total electron content, *Reviews of Geophysics*, *44*(4), 1–47, https://doi.org/10.1029/2005rg000193.

Nayar, S. R. P., V. N. Radhika, and P. T. Seena (2006), Investigation of substorms during geomagnetic storms using wavelet techniques, in *Proceedings of the ILWS Workshop*, pp. 19–24, Provided by the SAO/NASA Astrophysics Data System, Goa, India.

Otsuka, Y., T. Ogawa, A. Saito, T. Tsugawa, S. Fukao, and S. Miyazaki (2002), A new technique for mapping of total electron content using GPS network in Japan, *Earth, Planets and Space*, *54*(1), 63–70, https://doi.org/10.1186/bf03352422.

Panda, S. K., S. S. Gedam, and S. Jin (2015), Ionospheric TEC Variations at low Latitude Indian Region, in *Satellite Positioning - Methods, Models and Applications*, pp. 149–174, InTech, Rijeka, Croatia, https://doi.org/10.5772/59988.

Podobnik, B., and H. E. Stanley (2008), Detrended cross-correlation analysis: a new method for analysing two nonstationary time series, *Physical Review Letters*, *100*(8), 084,102, https://doi.org/10.1103/physrevlett.100.084102.

Podobnik, B., I. Grosse, D. Horvatić, S. Ilic, P. C. Ivanov, and H. E. Stanley (2009), Quantifying cross-correlations using local and global detrending approaches, *The European Physical Journal B*, *71*(2), 243–250, https://doi.org/10.1140/epjb/e2009-00310-5.

Poudel, P., N. Parajuli, A. Gautam, D. Sapkota, H. Adhikari, B. Adhikari, A. Silwal, S. P. Gautam, M. Karki, and R. K. Mishra (2020), Wavelet and Cross-Correlation Analysis of Relativistic Electron Flux with Sunspot Number, Solar Flux, and Solar Wind Parameters, *Journal of Nepal Physical Society*, *6*(2), 104–112, https://doi.org/10.3126/jnphyssoc.v6i2.34865.

Pulinets, S. A., A. Leyva-Contreras, G. Bisiacchi-Giraldi, and C. Ciraolo (2005), Total electron content variations in the ionosphere before the Colima, Mexico, earthquake of 21 January 2003, *Geofisica Internacional*, *44*(4), 369–377, https://doi.org/10.22201/igeof.00167169p.2005.44.4.237.

Rastogi, R. G., and J. A. Klobuchar (1990), Ionospheric electron content within the equatorial F2 layer anomaly belt, *Journal of Geophysical Research*, *95*(A11), 19,045–19,052, https://doi.org/10.1029/ja095ia11p19045.

Rostoker, G. (1972), Geomagnetic indices, *Reviews of Geophysics*, *10*(4), 935–950, https://doi.org/10.1029/rg010i004p00935.

Schrijver, C. J., K. Kauristie, A. D. Aylward, C. M. Denardini, S. E. Gibson, A. Glover, N. Gopalswamy, M. Grande, M. Hapgood, D. Heynderickx, N. Jakowski, V. V. Kalegaev, G. Lapenta, J. A. Linker, S. Liu, C. H. Mandrini, I. R. Mann, T. Nagatsuma, D. Nandy, T. Obara, T. P. O'Brien, T. Onsager, H. J. Opgenoorth, M. Terkildsen, C. E. Valladares, and N. Vilmer (2015), Understanding space weather to shield society: A global road map for 2015–2025 commissioned by COSPAR and ILWS, *Advances in Space Research*, *55*(12), 2745–2807, https://doi.org/10.1016/j.asr.2015.03.023.

Shadrina, L. P. (2017), Two types of geomagnetic storms and relationship between Dst and AE indexes, in *E3S Web of Conferences*, vol. 20, edited by B. Shevtsov, I. Myagkova, and V. Kozlov, p. 01010, EDP Sciences, https://doi.org/10.1051/e3sconf/20172001010.

Sharma, G., P. K. C. Ray, S. Mohanty, P. K. R. Gautam, and S. Kannaujiya (2017), Global navigation satellite system detection of preseismic ionospheric total electron content anomalies for strong magnitude (Mw< 6) Himalayan earthquakes, *Journal of Applied Remote Sensing*, *11*(04), 046,018, https://doi.org/10.1117/1.jrs.11.046018.

Sharma, S., P. Galav, N. Dashora, S. Alex, R. S. Dabas, and R. Pandey (2011), Response of low-latitude ionospheric total electron content to the geomagnetic storm of 24 August 2005, *Journal of Geophysical Research: Space Physics*, *116*(A5), https://doi.org/10.1029/2010ja016368.

Sharma, S. K., A. K. Singh, S. K. Panda, and S. S. Ahmed (2020), The effect of geomagnetic storms on the total electron content over the low latitude Saudi Arab region: a focus on St. Patrick's Day storm, *Astrophysics and Space Science*, *365*(2), 1–10, https://doi.org/10.1007/s10509-020-3747-1.

Shinbori, A., Y. Otsuka, T. Sori, T. Tsugawa, and M. Nishioka (2020), Temporal and spatial variations of total electron content enhancements during a geomagnetic storm on 27 and 28 September 2017, *Journal of Geophysical Research: Space Physics*, *125*(7), 1–21, https://doi.org/10.1029/2019ja026873.

Silwal, A., S. P. Gautam, K. Chaudhary, M. Khanal, S. Joshi, S. Dangaura, and B. Adhikari (2021a), Study of Solar Wind Parameters During Geomagnetic Storm of 26th August 2018 and 28th September 2017, *Thai Journal of Physics*, *38*(2), 54–68.

Silwal, A., S. P. Gautam, P. Poudel, M. Karki, B. Adhikari, N. P. Chapagain, R. K. Mishra, B. D. Ghimire, and Y. Migoya-Orue (2021b), Global positioning system observations of ionospheric total electron content variations during the 15 January 2010 and 21 June 2020 solar eclipse, *Radio Science*, *56*(5), 1–20, https://doi.org/10.1029/2020rs007215.

Sori, T., A. Shinbori, Y. Otsuka, T. Tsugawa, and M. Nishioka (2019), Characteristics of GNSS total electron content enhancements over the midlatitudes during a geomagnetic storm on 7 and 8 November 2004, *Journal of Geophysical Research: Space Physics*, *124*(12), 10,376–10,394, https://doi.org/10.1029/2019ja026713.

Sreeja, V., C. V. Devasia, S. Ravindran, T. K. Pant, and R. Sridharan (2009), Response of the equatorial and low-latitude ionosphere in the Indian sector to the geomagnetic storms of January 2005, *Journal of Geophysical Research: Space Physics*, *114*(A6), 1–13, https://doi.org/10.1029/2009ja014179.

Tsugawa, T., M. Nishioka, M. Ishii, K. Hozumi, S. Saito, A. Shinbori, Y. Otsuka, A. Saito, S. M. Buhari, M. Abdullah, and P. Supnithi (2018), Total electron content observations by dense regional and worldwide international networks of GNSS, *Journal of Disaster Research*, *13*(3), 535–545, https://doi.org/10.20965/jdr.2018.p0535.

Tsurutani, B., A. Mannucci, B. Iijima, M. A. Abdu, J. H. A. Sobral, W. Gonzalez, and V. M. Vasyliunas (2004), Global dayside ionospheric uplift and enhancement associated with interplanetary electric fields, *Journal of Geophysical Research*, *109*(A8), 1–16, https://doi.org/10.1029/2003ja010342.

Usoro, A. E. (2015), Some basic properties of cross-correlation functions of n-dimensional vector time series, *Journal of Statistical and Econometric Methods*, *4*(1), 63–71.

Vichare, G., R. Rawat, A. Hanchinal, A. K. Sinha, A. Dhar, and B. M. Pathan (2012), Seasonal evolution of S q current system at sub-auroral latitude, *Earth, Planets and Space*, *64*(11), 1023–1031, https://doi.org/10.5047/eps.2012.04.007.

Yao, Y., X. Chen, J. Kong, C. Zhou, L. Liu, L. Shan, and Z. Guo (2021), An Updated Experimental Model of IG12 Indices Over the Antarctic Region via the Assimilation of IRI2016 With GNSS TEC, *IEEE Transactions on Geoscience and Remote Sensing*, *59*(2), 1700–1717, https://doi.org/10.1109/tgrs.2020.2999132.

Yasyukevich, Y., E. Astafyeva, A. Padokhin, V. Ivanova, S. Syrovatskii, and A. Podlesnyi (2018), The 6 September 2017 X-class solar flares and their impacts on the ionosphere, GNSS, and HF radio wave propagation, *Space Weather*, *16*(8), 1013–1027, https://doi.org/10.1029/2018sw001932.

Yokoyama, N., and Y. Kamide (1997), Statistical nature of geomagnetic storms, *Journal of Geophysical Research: Space Physics*, *102*(A7), 14,215–14,222, https://doi.org/10.1029/97ja00903.

Zhang, W., X. Zhao, S. Jin, and J. Li (2018), Ionospheric disturbances following the March 2015 geomagnetic storm from GPS observations in China, *Geodesy and Geodynamics*, *9*(4), 288–295, https://doi.org/10.1016/j.geog.2018.02.001.